CrossMark

Trigger of Successive Filament Eruptions Observed by SDO and STEREO

Sajal Kumar Dhara[1,2] · Ravindra Belur[3] ·
Pankaj Kumar[4,5] · Ravinder Kumar Banyal[3] ·
Shibu K. Mathew[1] · Bhuwan Joshi[1]

Abstract Using multiwavelength observations from the *Solar Dynamics Observatory*
(SDO) and the *Solar Terrestrial Relations Observatory* (STEREO), we investigate the mechanism of two successive eruptions (F1 and F2) of a filament in active region NOAA 11444
on 27 March 2012. The filament was inverse J-shaped and lay along a quasi-circular polarity
inversion line (PIL). The first part of the filament erupted at $\sim$ 2:30 UT on 27 March 2012
(F1), the second part at around 4:20 UT on the same day (F2). A precursor or preflare brightening was observed below the filament main axis about 30 min before F1. The brightening
was followed by a jet-like ejection below the filament, which triggered its eruption. Before
the eruption of F2, the filament seemed to be trapped within the overlying arcade loops
for almost 1.5 h before it successfully erupted. Interestingly, we observe simultaneously
contraction ($\sim$ 12 km s^{-1}) and expansion ($\sim$ 20 km s^{-1}) of arcade loops in the active region
before F2. Magnetograms obtained with the *Helioseismic and Magnetic Imager* (HMI) show
converging motion of the opposite polarities, which result in flux cancellation near the PIL.
We suggest that flux cancellation at the PIL resulted in a jet-like ejection below the filament
main axis, which triggered F1, similar to the tether-cutting process. F2 was triggered by
removal of the overlying arcade loops *via* reconnection. Both filament eruptions produced
high-speed ($\sim$ 1000 km s^{-1}) coronal mass ejections.

✉ S.K. Dhara
sajal@irsol.ch

1   Udaipur Solar Observatory, Physical Research Laboratory, Dewali, Badi Road, Udaipur 313 004,
     India

2   Istituto Ricerche Solari Locarno associated to Università della Svizzera Italiana, Locarno-Monti,
     Switzerland

3   Indian Institute of Astrophysics, II Block, Koramangla, Bangalore 560034, India

4   Korea Astronomy and Space Science Institute (KASI), Daejeon, 305-348, South Korea

5   Heliophysics Science Division, NASA Goddard Space Flight Center, Greenbelt MD 20771, USA

 Springer

1. Introduction

Filaments or prominences are chromospheric and coronal structures that contain relatively cool, dense plasma that is suspended along polarity inversion lines (PILs). Flares and coronal mass ejections (CMEs) are often associated with filament eruptions (Schmieder *et al.*, 2002; Gopalswamy *et al.*, 2003), which eventually affect space weather. The fundamental processes responsible for these eruptions originate in the magnetic field of the solar atmosphere (Priest and Forbes, 2002).

According to a filament/prominence eruption model (e.g. van Ballegooijen and Martens, 1989), the filament mass is supported in the dips of the helical field lines. To understand the relation between the filament mass and the corresponding supporting magnetic structure, Gilbert, Alexander, and Liu (2007) categorized filament eruptions observationally as "full", "partial", and "failed" eruptions, depending on the site of magnetic reconnection. In the case of a full eruption, the reconnection takes place below the flux rope and most of the filament mass ($\geq 90\%$) escapes along with the entire flux rope structure. For a failed eruption, reconnection occurs above the flux rope, which pushes the filament downward. In the case of a partial eruption, reconnection may occur within the filament material. This leads to the eruption of a portion of the filament.

Several observations show that activity occurring near the filament is important during its pre-eruption phase. Small-scale magnetic reconnection occurring during the pre-eruptive phase may trigger flares, which involves a large-scale reorganization of the magnetic connectivity (*e.g.* Toriumi *et al.*, 2013; Kusano *et al.*, 2012). Therefore, it is very important to know the location and height of the small-scale reconnection sites. Several models have been proposed to examine the role of the initial magnetic reconnection. These models set up the conditions that are favorable for the magnetic core fields to erupt. One of the mechanisms is tether cutting, in which explosive reconnection occurs within the twisted and deeply sheared core field of a bipole above the PIL of the arcade (Moore and Roumeliotis, 1992; Moore and Labonte, 1980; Moore *et al.*, 2001). In this model magnetic reconnection occurs in such a way that it forms a flux rope and also triggers the eruption. Initially, filaments often show a relatively slow rising motion before the onset of eruptions (Kahler *et al.*, 1988; Liewer *et al.*, 2009; Nagashima *et al.*, 2007; Sterling, Harra, and Moore, 2007; Xu, Jing, and Wang, 2010; Sterling, Moore, and Freeland, 2011). This early slow rise motion is considered as one of the reasons that trigger the eruption (Moore and Sterling, 2006; Sterling, Harra, and Moore, 2007; Sterling *et al.*, 2010). A transient brightening at or near the PIL, coincident with emerging and/or canceling magnetic flux, has been observed and is considered a precursor of the flare and filament eruption (Martin, 1980; Chifor *et al.*, 2007; Kim *et al.*, 2007; Liu *et al.*, 2009; Sterling, Moore, and Freeland, 2011).

Antiochos, DeVore, and Klimchuk (1999) proposed the breakout model, in which the topology of the photospheric magnetic field is quadrupolar and plays a crucial role for the CME initiation. The basic idea of this model is that magnetic reconnection at a null point in the corona above a sheared neutral line removes the constraint of the higher magnetic flux that tends to hold down the sheared low-lying field. This constraint removal forces the sheared core field to erupt explosively outward (Antiochos, 1998; Antiochos, DeVore, and Klimchuk, 1999; Karpen, Antiochos, and DeVore, 2012). In the context of these two

models, the role of magnetic reconnection for the eruption can be investigated during the pre-eruption phase.

Magnetic reconnection can also occur at a low level in the solar atmosphere (*e.g.* Wang and Shi, 1993). It may be observed at the photosphere as a cancellation of magnetic features (Priest, Parnell, and Martin, 1994). Flux cancellation (Martin, Livi, and Wang, 1985) is the process where the magnetic flux disappears at the PIL, as formulated by van Ballegooijen and Martens (1989). Flux cancellation at the PIL can lead the coronal structure to evolve towards highly sheared fields that can eventually erupt (Green, Kliem, and Wallace, 2011). A gradual flux cancellation that continues over an extended period can trigger the filament eruption (*e.g.* Sterling *et al.*, 2010; Zuccarello *et al.*, 2007).

Filament eruptions occur on a timescale that is much shorter than the timescale of coronal magnetic energy accumulation, hence there should be a magnetohydrodynamic (MHD) instability related to the trigger of the eruption. Therefore, different instability mechanisms have been evoked (see the review by Forbes, 2000). Numerical MHD simulations of the kink instability suggest that if the twist of the flux rope exceeds a critical value, then the flux rope becomes unstable (*e.g.* Hood and Priest, 1979; Török and Kliem, 2003; Török, Kliem, and Titov, 2004). This value depends on the aspect ratio of the loop and on the ratio of the plasma to magnetic pressure. Previous observational studies support the hypothesis that the kink instability is the trigger mechanism for solar eruptions (*e.g.* Srivastava *et al.*, 2010; Kumar *et al.*, 2012; Kumar and Cho, 2014). One example of a filament eruption studied by Yan *et al.* (2014) in active region (AR) NOAA 11485 showed that the leg of the filament rotated up to 2.83π around the axis of the filament with a maximum rotation speed of 100 degrees *per* minute. This study indicates that the kink instability is the trigger mechanism for the solar filament eruption.

The filament or flux rope can experience another type of instability called torus instability (*e.g.* Kliem and Török, 2006; Zuccarello *et al.*, 2014; Dhara, Ravindra, and Banyal, 2014). Some pre-eruptive processes, such as flux cancellation or emergence at the neutral line and magnetic reconnection during observed brightenings, initiate the eruption by bringing the flux rope to a height. Using MHD numerical simulations of a flux rope that emerged from the subsurface into the magnetized corona in a 3D spherical geometry, Fan and Gibson (2007) found that when the background magnetic field decreases slowly with height, a strongly twisted flux tube that emerges from the solar surface can rupture the arcade field through kink instability. When the background magnetic field decreases rapidly with height, however, the flux rope can become unstable to the lateral expansion, and then it erupts. This type of loss of equilibrium can be interpreted as a torus instability (Chen, 2011). In this model, a current ring of major radius, R, is embedded in an external magnetic field, B_{ex}. The current rings are subjected to a radially outward-directed hoop force. When the ring expands, the hoop force decreases. If the inward-directed Lorentz force that is due to the external field, B_{ex}, decreases faster with R than the hoop force, the system is unstable to perturbations. The decay index for a current ring of major radius R and embedded in an external field B_{ex} is defined as follows (Zuccarello *et al.*, 2014):

$$n = -R\frac{d}{dR}(\ln B_{ex}). \tag{1}$$

Assuming an external magnetic field $B_{ex} \propto R^{-n}$, Bateman (1978) numerically showed that such an instability will occur when $n > n_{critical} = 1.5$.

In this article, we study the origin of two successive filament eruptions (F1 and F2) that occurred in AR NOAA 11444, observed by the *Solar Dynamics Observatory* (SDO) and the *Solar Terrestrial Relations Observatory* (STEREO). We discuss the important morphological changes in and around the filament before the eruptions and the possible trigger

mechanism. This article is organized as follows. In Section 2 we describe the different instruments and data used in this study. A brief description of the filament and the sequence of the events in the corona, chromosphere, and at the photosphere are presented in Section 3. Finally, we discuss our results in Section 4.

2. Instruments and Data

We used the EUV images obtained with the *Atmospheric Imaging Assembly* (AIA: Lemen *et al.*, 2012) onboard the SDO (Pesnell, Thompson, and Chamberlin, 2012) to study the filament eruption in detail. In particular, we have used data obtained in the AIA 171, 193, and 304 Å channels that correspond to the corona and chromosphere. We used level 1.0 data and the *aia_prep.pro* routine available in the SolarSoftware package to coalign the images from all of the AIA channels. From these datasets, the filament regions were extracted and tracked over time. These images are obtained with a cadence of 12 seconds and a pixel resolution of 0.6″. We acquired the data starting from 22:00 UT on 26 March 2012 until 07:00 UT on 27 March 2012, which covers the activation of the filament eruption and subsequent runaway motion for the entire event. To study the filament eruption above the solar limb, we also used images obtained with the *Extreme Ultaviolet Imager* (EUVI) in 304 and 195 Å from the *Sun-Earth Connection Coronal and Heliospheric Investigation* (SECCHI: Howard *et al.*, 2008) onboard STEREO A (Kaiser *et al.*, 2008). The EUVI 2048 × 2048 pixel detectors have a field of view out to 1.7 solar radii, which completely covered this filament eruption event.

The morphology of the filament at chromospheric heights can be studied with Hα images. We analyzed full-disk Hα images from the *Global Oscillation Network Group* (GONG: Harvey *et al.*, 1996). GONG collects Hα images at six sites around the world. The dark, flat, smear-corrected, and compressed Hα images are available with a cadence of almost one minute. These Hα images are obtained with a 2048 × 2048 pixel CCD camera whose pixel resolution is about 1″. We analyzed Hα images starting from 23:00 UT on 26 March 2012 until 06:00 UT on 27 March 2012. The dataset covers the first and second eruption of the filament and subsequent flares.

In order to examine the changes in the photospheric magnetic field near the filament footpoints, we used the full-disk line-of-sight magnetograms at level 1.0 from the *Helioseismic and Magnetic Imager* (HMI: Scherrer *et al.*, 2012) with a cadence of 45 seconds. The line-of-sight magnetogram has a pixel resolution of 0.5″. We used the *aia_prep.pro* routine to upgrade the HMI magnetogram to level 1.5 so as to interpolate to the AIA pixel resolution. We have tracked the region of interest *ROI* by using the heliographic coordinate information and finally corrected for the line-of-sight effect by multiplying $1/\cos\theta$, where θ is the heliocentric angle. We then averaged four magnetograms to reduce the noise level (Liu *et al.*, 2012) to about 10 G. These magnetograms were used to study the evolution of magnetic fields in and around the filament at the photospheric level.

3. Observations and Results

3.1. AIA Observations of the Filament Eruption

The filament was observed in AR NOAA 11444 at the location N19 E26 on 23 March 2012 and survived for almost three days. On 27 March 2012, before the eruption, the filament
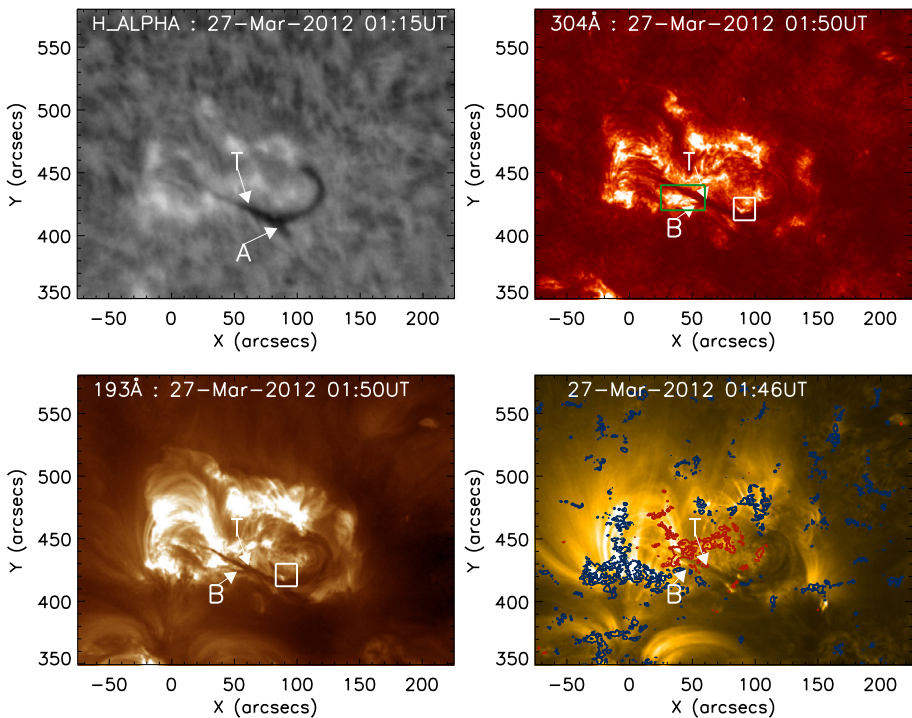
Figure 1 Filament observed in Hα (*top-left panel*), AIA 304 Å (*top-right panel*), 193 Å (*bottom-left*), and 171 Å (*bottom-right panel*). The filament location is shown by the *white arrow* with the letter T. The *arrow* with the letter B shows a bifurcation of the filament below T. The *arrow* with the letter A in the Hα image shows the location of the protrusion that appears as a barb of the filament. The region within the *white box* in 304 and 193 Å images shows the jet location close to the filament. The region within the *green box* in the *top-right panel* shows the location of the preflare brightening in 304 Å image. The contours of the magnetic field are overlaid on the 171 Å image. The *red* and *blue contours* represent positive and negative polarities with magnetic field strength values of ±100, 150, 200, and 250 G.

was observed at the heliographic position N21 W17. The filament appears to have an inverse J-shape in the Hα (top-left panel), He II 304 (top-right panel), 193 Å (bottom-left panel), and 171 Å (bottom-right panel) images in Figure 1, respectively. The arrow followed by the letter T in Figure 1 shows the filament, and the arrow followed by the letter A in the Hα image indicates the location of the protrusion that appears as a barb. The appearances of the filament in the coronal images (193 and 171 Å) are also shown in Figure 1 (bottom left and right panels, respectively). The filament followed the polarity inversion line (PIL). The northern end of the filament was rooted in a compact negative-polarity plage region, and the southern portion ended in the positive-polarity plage. The axial field component of the filament is right bearing when we look at the filament from the positive-polarity side. This corresponds to a dextral chirality and is consistent with hemispheric helicity rule (Martin, 1998; Martin, Bilimoria, and Tracadas, 1994). This was confirmed later in the erupting filament. The erupting filament (shown in Figure 2) shows a crossing of dark and bright threads in 171 Å image. The crossing of dark features over the bright regions is easily identified in the zoomed image, where a bright feature in the background is seen that extends from left to right, while the dark feature in the foreground crosses it from right to left. These crossing threads correspond to a negative mutual (type III) helicity (Chae, 2000).

Figure 2 Erupting filament shown in the 171 Å channel. The *two arrows* indicate the crossing of dark threads over bright threads. The *box in the top-right corner* of the image shows the zoomed-in version of the threads.
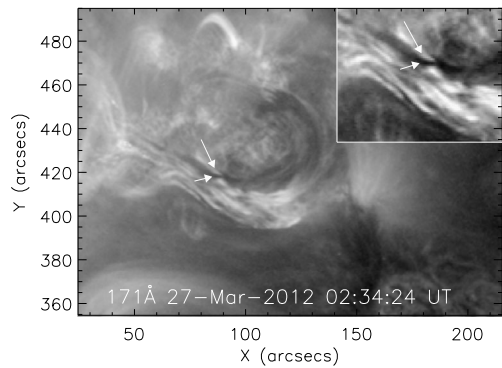
The filament seems to have two structures. One is a broad inverse J-shaped structure that is visible in the Hα 6563 Å, AIA 171, 193, and 304 Å wavelengths. This filament region is shown by an arrow with the letter T, indicating a filament at the top. One more thin filament lies below the top filament or a bifurcation of the main filament, shown by an arrow with the letter "B". It appears to start $\sim 35''$ in the horizontal direction and $\sim 425''$ in the vertical direction in EUV images. It bends down at $\sim 45''$ and later continues with the main T filament, also having a inverse J-shape. The bottom side or bifurcated filament is shown by the letter B in Figure 1.

In order to study the filament eruption in detail, we created an online movie[1] of the erupting filament in the 304 and 171 Å channels of AIA. The movie clearly shows that the filament erupted in two stages. In the first stage, the southern part of the filament erupted. This eruption was followed by a C5.3 class flare identified by GOES detector at $\sim 02:52$ UT. The second eruption was initiated at around 3:50 UT. In this eruption, the northern part of the filament erupted and accelerated at 4:20 UT, followed by a C1.7 class flare at $\sim 04:25$ UT.

The contours of the photospheric magnetic field overlaid on the 171 Å images, shown in Figure 1 (bottom-right panel), indicate that the filament lies along the neutral line. The southern portion of the filament ended in the bipolar regions where flux cancellation was observed. The jet in the cusp-shaped region observed close to the filament is enclosed in a white box in the 304 and 193 Å wavelength images in Figure 1. Over a period of 2.5 h starting from 00:00 UT to 02:30 UT (on 27 March 2012), jets are repeatedly observed in this region. The photospheric magnetograms showed repeated emergences and cancellations of magnetic flux at the same site. Figure 3 shows the sequence of line-of-sight magnetograms for the same location at different times during the jet observations. The emergence and cancellation of magnetic flux regions is marked by circles in the time sequence of the magnetograms.

3.2. Pre-Flare Brightening and Filament Eruptions

A brightening was observed starting at 01:56 UT below the filament T. The brightening location is shown in the 304 Å channel by a green box in Figure 1 (top-right panel). The brightening was followed by a bright plasma flow that moved from the east end of the filament to the west. During the flow, the filament appeared as a sequence of bright and dark

---

[1]Movies (AIA_304.avi and AIA_171.avi) generated from SDO/AIA 171 and 304 Å images, respectively, of the filament eruption associated with AR NOAA 11444 are available in the electronic version of the manuscript.
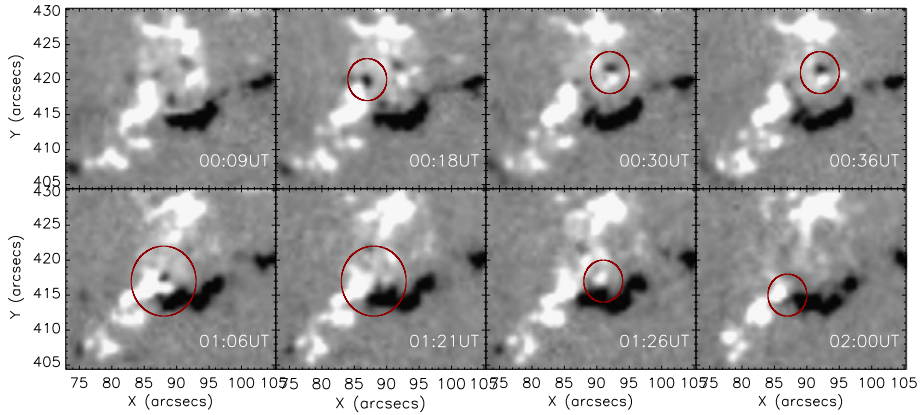
Figure 3 Sequence of the line-of-sight magnetograms showing the location of the jet seen in the white box in Figure 1. The *white* and *black region* represent the positive and negative polarities, respectively. The locations of flux cancellations and emergence are shown by *circles*.

Figure 4 Sequence of STEREO-A/EUVI 304 Å (*top panels*) and 195 Å (*bottom panels*) images showing the eruption of a filament (F1). The *arrow* indicated by the letter E in 304 Å image shows the upward plasma flow or jet before the eruption of F1.
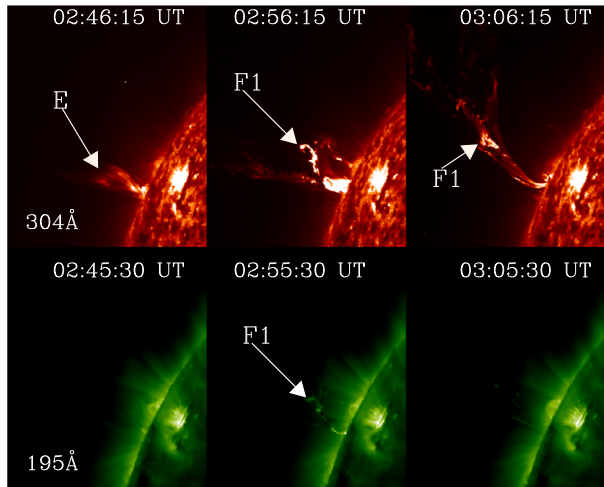
threads. The bright flow reached the barb location at 02:03 UT. During that time, the bifurcated filament (B) moved up slightly, and the top filament (T) lifted as well. At around 2:35 UT, the separation between the bright and dark threads of the filament became large, and on the west side, one end of the filament started to move upward. At around 2:53 UT, there was a C5.3 class flare, and during this time, a large amount of bright mass was ejected along with the filament eruption (F1). Figure 4 shows the sequence of STEREO-A/EUVI 304 Å and 195 Å images during the eruption of F1. The first panel of Figure 4 (top) shows the bright upward flow or jet that is seen in 304 Å images before the eruption. The middle and last panels show the eruption of the filament. The estimated speed of the filament eruption (F1), computed from 304 Å images, is 274 ± 11 km s^{-1}. The formation of a close underlying flare loop, observed in the 195 Å image during the jet, suggests that the magnetic reconnection is the driver of the jet and the associated filament eruption.

Soon after the eruption of F1, we observed the activation of filament F2, which does not erupt and remains stationary for a longer period. This filament (F2) is shown by an arrow in the 171 Å image in Figure 9 (top). At around 4:20 UT, this filament also started to erupt, followed by a C1.7 class flare. The filament disappeared from the field of view at around 4:30 UT in the AIA 171 Å images.

3.3. Temporal Evolution of Filament Eruptions and Flares

To investigate the temporal evolution of the successive filament eruptions and associated flare activities, we constructed time-distance (TD) maps from a series of AIA 304 and 171 Å images starting from 01:00 UT on 27 March 2012. The TD map for the first filament eruption is extracted from slit-I and the second eruption is extracted from slit-II (shown in the top panel of Figure 5). The TD maps shown in Figure 5 are extracted from 304 and 171 Å images. The position of the filament in the TD map generated from 304 Å images (middle-left image) is shown by an arrow labeled A. There was a pre-flare brightening close to the filament at $\sim$ 01:56 UT. The location of the brightening in the TD map is highlighted by an arrow labeled Br. A similar brightening is also visible in the other TD map, generated from 171 Å images (bottom-left panel). The filament later showed a slow-rise motion at a projected speed of 1.5 ± 0.3 km s^{-1}. At around 2:30 UT, there was another brightening related to the C5.3 class flare. The filament rose faster during this time. This location is indicated by a vertical line close to the filament in the TD map. The flare maximum occurred at around 3:08 UT. The filament accelerated during the flare and erupted with a projected speed of 130 ± 3 km s^{-1}.

The second filament F2 erupted in a different manner compared to the previous eruption. After its activation, the filament seemed to have a counter-clockwise motion and then moved away southward. This filament accelerated and erupted with a projected speed of 37 ± 2 km s^{-1}. This event was followed by the C1.7 class flare. Figure 6 shows the sequence of STEREO-A/EUVI 304 Å and 195 Å images during the eruption of the filament (F2) in its second phase. The speed during the eruption of F2 on the sky plane estimated from these 304 Å images was about 145 ± 10 km s^{-1}.

Figure 7 (bottom panel) shows the intensity profiles in the AIA 171, 304, 131, and 193 Å channels. The pre-flare brightening was observed below the filament. The light curves were obtained by integrating the intensity in a small region (green box) shown in the AIA 304 Å image (Figure 1, top-right panel). The light curves show a small rise at around 01:56 UT in the region within the box. The TD maps indicate that the filament activation started at the same time. Later, at around 2:50 UT, there was a jump in the GOES X-ray curve in the $1.0 - 8.0$ Å band. At the same time, we observed a jump in intensity for all the 304, 131, 171, and 193 Å wavelengths. Therefore, the EUV and X-ray flux profiles are consistent. The brightening in the GOES and in other EUV wavelengths reached the background level over a period of about 40 min after the flare. During the initiation of the C5.3 flare, the filament showed an acceleration and eventual eruption. Interestingly, GOES soft X-ray flux profiles reveal a small B-class flare (peak around 03:56 UT) between these two filament eruptions. However, this cannot be distinguished in the EUV light curves. This flare was associated with the eruption of an overlying arcade before the successful eruption of filament F2.

3.4. Contraction of a Coronal Loop in the First Phase

Just a few minutes before the eruption F1, there was a contraction of a coronal loop in the eastern part of the filament. The loop contraction was observed during $2:32 - 2:35$ UT.
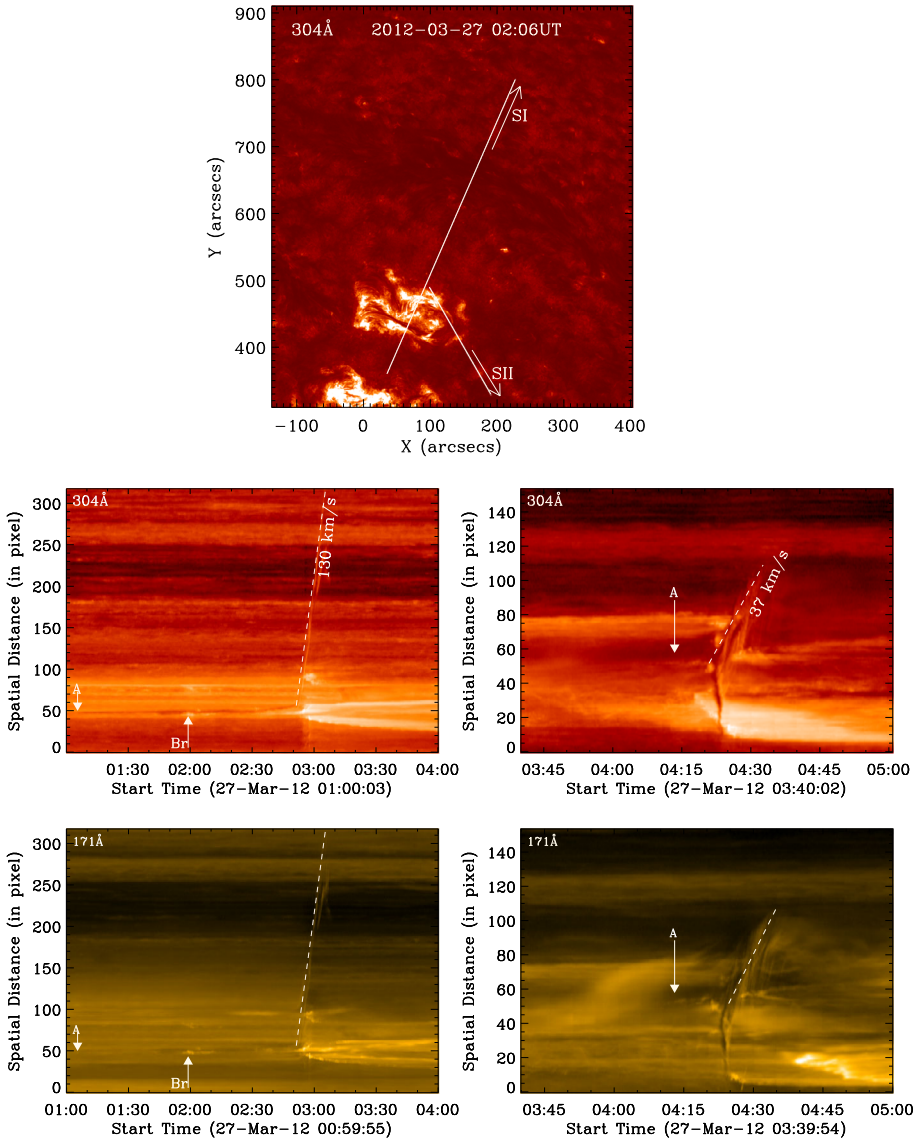
Figure 5 Two filament eruptions in the AIA observations. *Top*: AIA 304 Å image showing the filament. Two *white lines* or slits overlaid on the image represent the positions from which we generated the time-distance maps. Slit I traces the first eruption of the filament (F1), while slit II traces the second eruption (F2). *Middle*: space–time map of the filament eruption for slit I (*left*) and for slit II (*right*) extracted from 304 Å images. *Bottom*: space–time map of filament eruption for slit I (*left*) and for slit II (*right*) extracted from 171 Å images. A dark bent portion of the filament represents the path of the filament while it erupted. The *white arrow* followed by the letter A (*left images*) shows the initial position of the filament before eruption. The second *white arrow* followed by Br shows the brightening during the eruption.

Figure 8 (panels in the first row) shows the contraction with time of the coronal loop in a sequence of 171 Å images. A zoom of the contracting loop regions (region within the blue box) is shown in Figure 8 (panel in the second row) for the same hours as the images in the

Figure 6 Sequence of STEREO-A/EUVI 304 Å (*top panel*) and 195 Å (*bottom panel*) images showing the filament eruption (F2).
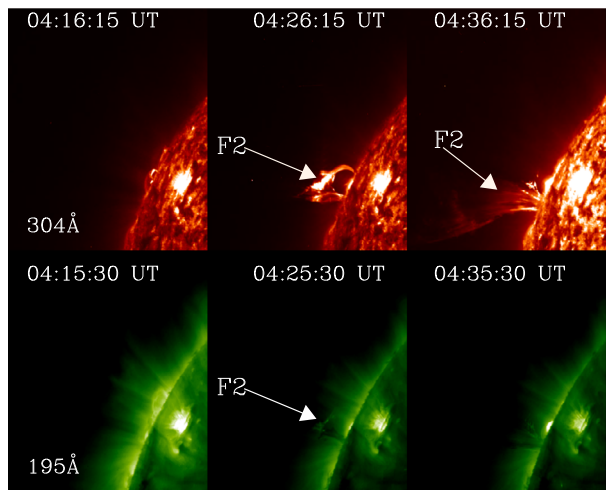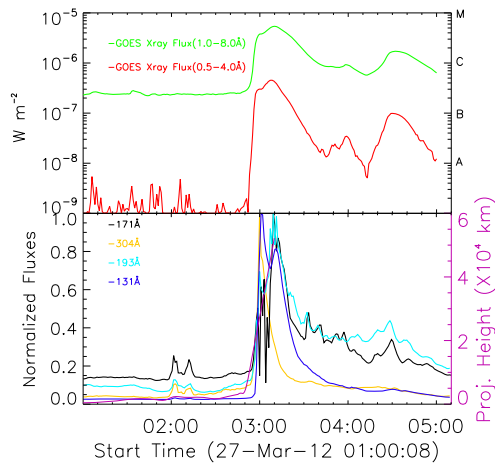

Figure 7 GOES and AIA light curves including the eruptions. *Top*: GOES soft X-ray flux profiles in the 1 – 8 and 0.5 – 4 Å channels. *Bottom*: normalized fluxes plotted for the AIA 171 Å, 193 Å, 304 Å, and 131 Å channels. The projected time-distance plot for eruption F1 is also included in the *right vertical axis*.

first row. The time sequence of high-pass filtered 171 Å images for the contracting loop are shown in the two bottom rows of Figure 8 for better contrast; the second of these two rows is a zoom of the top row (blue box) for the same hours. These high-pass filtered images are obtained by using the wavelet transform (Young, 2007). The contracting loop is shown by an arrow in every image in both panels. During its collapse, it covered about $15''$ in height. Although its signature is not visible because its brightness decreased, we later see material falling onto the filament at 2:37 UT, indicating that the loop reached the filament location at that time. Soon after the collapse of the loop, the filament started to erupt.

3.5. Simultaneous Contraction and Expansion of Arcade Loops

After the first eruption (F1), the northwestern portion of the filament was activated. One of the post-flare loops started to shrink above the filament, which is shown by an arrow (L1) in Figure 9 (top row). The space–time plot along the slit (overlaid on Figure 9 in the first panel of the top row) shows the contraction of the loop. The space–time plot is shown in Figure 10
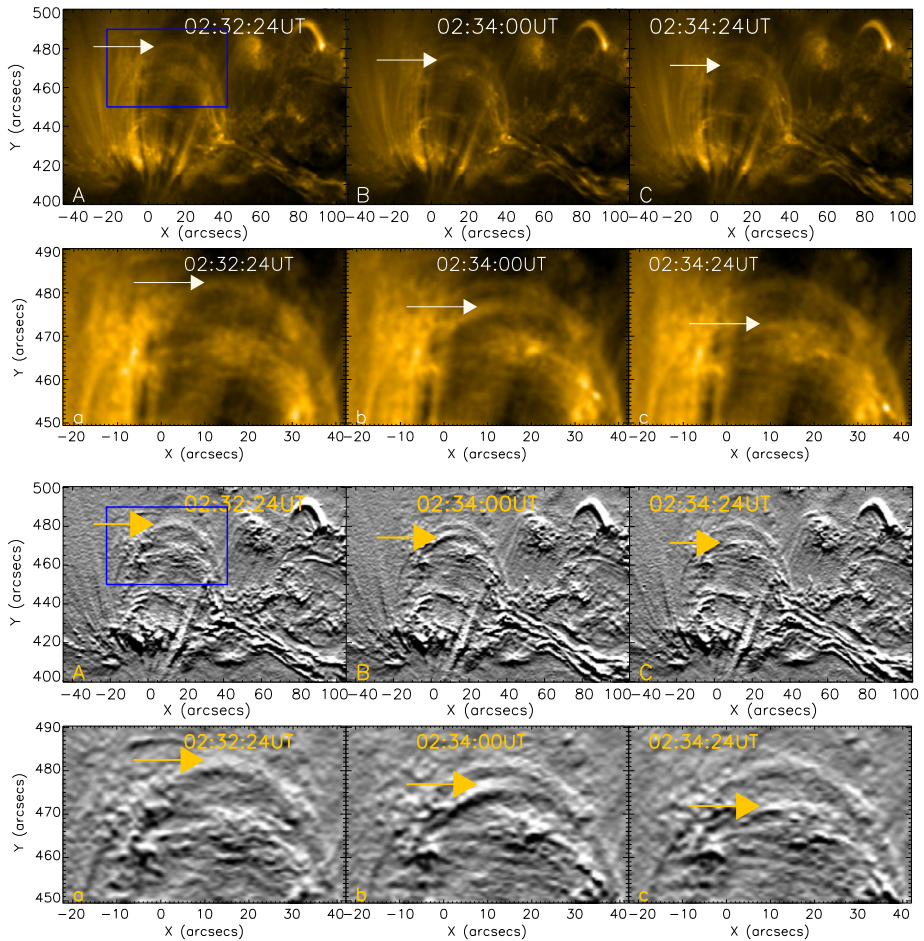
Figure 8 Images of the contracting loop. *Top row*: Sequence of 171 Å image (panels **A** – **C**) for the east portion of the filament just before the first eruption showing the contraction of the loop with time. The *white arrow* shows the bright loop which was contracting. *Second row*: Sequence of 171 Å images (panels **a** – **c**) (zoomed portion of the *blue box* in the *first row left image*) showing the contraction of the loop. *Third row*: Sequence of 171 Å high-pass filtered images (panels **A** – **C**) showing the contraction of the loop. *Fourth row*: Sequence of 171 Å high-pass filtered images (panels **a** – **c**) (zoomed portion of the *blue box* in the *first row left image*) showing the contraction of the loop.

(left). The filament (F2) and contracting loop (L1) are shown in this plot. The contracting loop was also visible in the AIA 193, 211, and 335 Å channels. The loop height decreased with time. After the shrinking loop disappeared in the AIA 171 Å channel, the dark material in the filament appeared to be moving westward at 3:40 UT. After this, several loops around the filament cooled down, and the length of the dark filament increased in size at 4:15 UT.

In the sequence of Hα images, the shrinking loop was not visible, but the motion of the dark material in the filament channel was visible with time. At 3:20 UT, a dark arc-shaped filament north of the two-ribbon flare was visible (see Figure 9 bottom row).

Near the east side of the filament, several loops were visible. At around 03:45 UT, there was a radially outward expansion of these loops in the active region, as shown in the se-
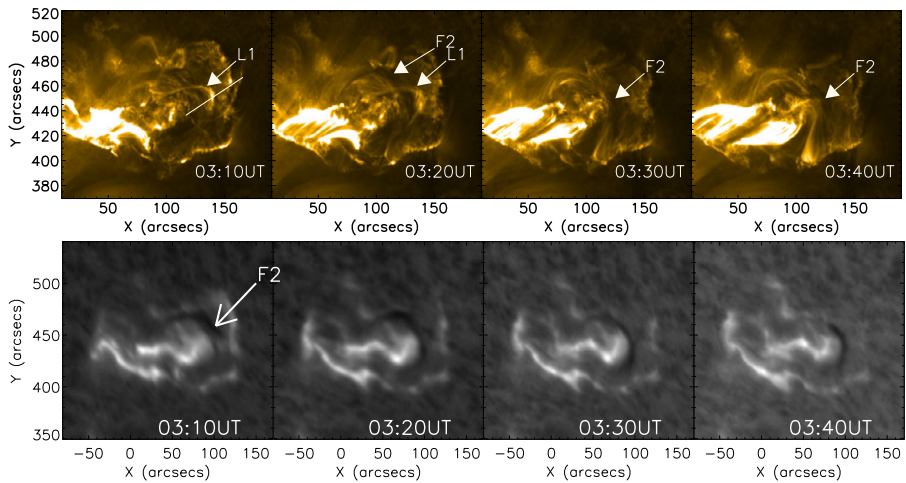
Figure 9 EUV and Hα images of the contraction of a post-flare loop. *Top*: Sequence of 171 Å images for the northwestern portion of the filament after the first eruption showing the contraction of one of the post-flare loops. The *white arrow* followed by L1 shows the bright loop which was contracting before the second activation. The *white arrow* followed by F2 indicates the filament location. *Bottom*: Sequence of H$_\alpha$ images showing the filament position with time by a *white arrow* (F2).
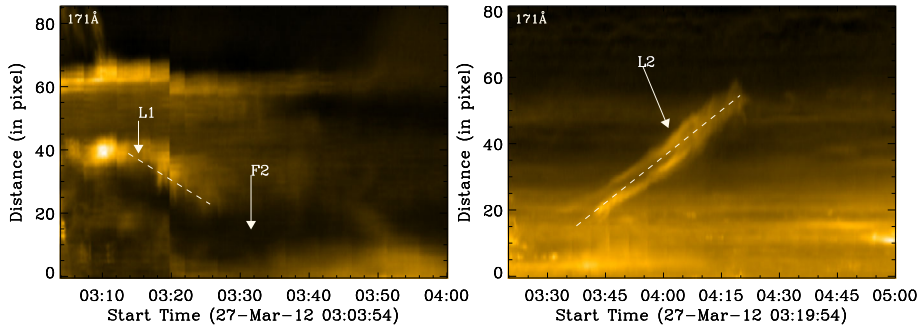

Figure 10 Contraction and expansion of arcade loops in 171 Å. *Left*: TD map of the contracting loop L1 along the slit of Figure 9 (*top row*, *first image*). The filament and loop locations are shown using *arrows* followed by the letters F2 and L1, respectively. The *white dashed line* represents the path along which the loops are contracted. *Right*: TD map of the expanding loop along the slit of Figure 11 (panel C). The *white dashed line* represents the path along which the loops expand.

quence of 171 Å images in Figure 11 (panels A–F). The arrow followed by L2 shows the expanding loops. A small brightening was observed at around 03:40 UT in the EUV in the eastern footpoint location of the expanding loop. This brightening location is shown by a blue rectangular box in Figure 11 (panels A and B) in the 171 Å channel.

In the brightening location, small-scale magnetic flux cancellation was observed (shown in the box region in Figure 12, panel A). The zoom of the box in panel A is also shown in Figure 12 (panels B–I) with time. In the magnified magnetograms, the circled region shows the canceling features where the positive-polarity region moved toward the negative-polarity region and eventually canceled.
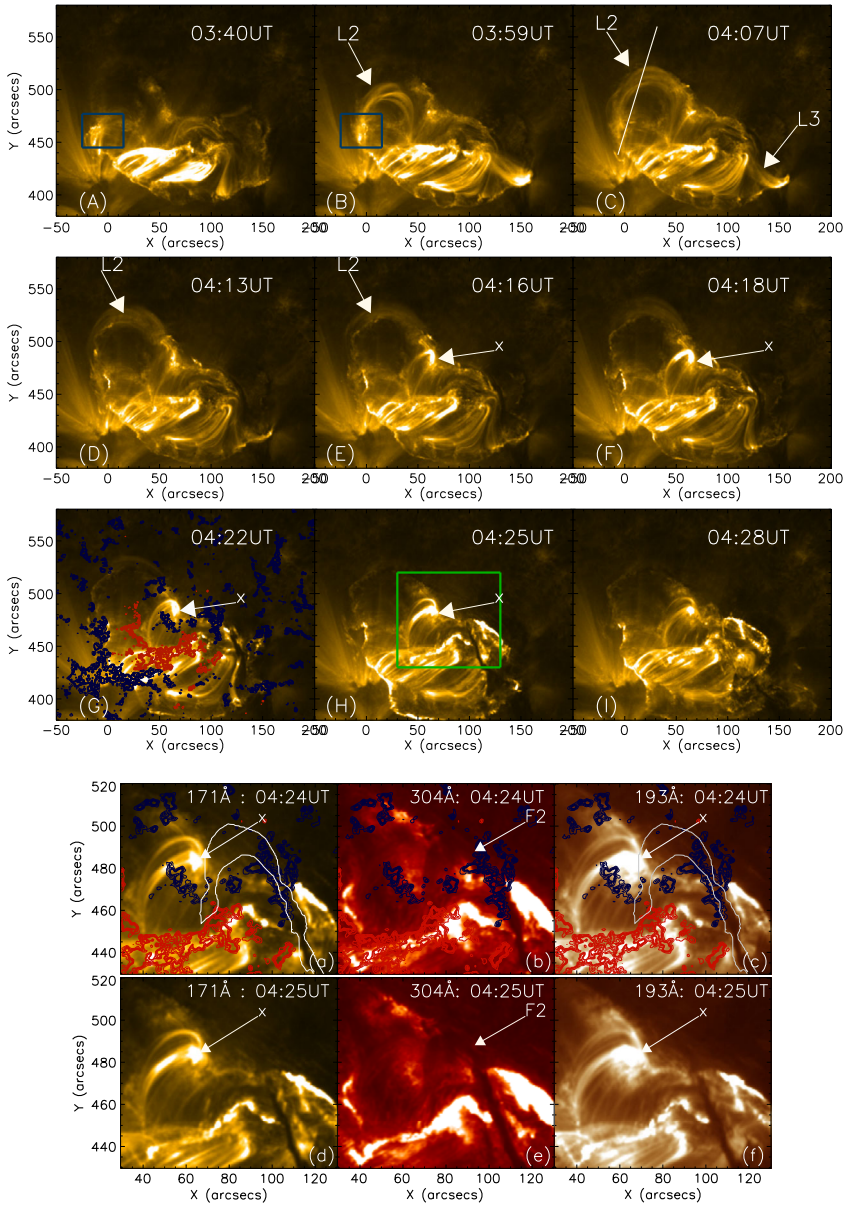
Figure 11 Panels **A – I**: Sequence of 171 Å images for the north-west portion of the filament before the second eruption showing the expansion and collapse of coronal loops. The *white arrows* L2 and L3 show the expansion and collapse of the coronal loops, respectively. The *white arrow* labeled as x in panels **E – H** shows the brightened loop close to eastern footpoint of the filament during filament activation. The *blue boxed region* (panels **A** and **B**) shows the brightening close to eastern footpoint of the expanding loops. The *red and blue contours* on panel **G** represent the positive and negative polarities with magnetic field strength values of ±50, 100, 150, 200 and 250 G, respectively. Panels **a – f**: Magnified version of the *green colored boxed region* of panel **H** shown in three different wavelengths 171, 304 and 193 Å, respectively. The brightened loops are shown by an *arrow* labeled as x in 171 and 193 Å images and the erupting filament is shown by the *arrow* labeled as F2 in the 304 Å image (panels **b** and **e**). The erupting filament contour overlaid on 171 and 193 Å images is extracted from 304 Å image.
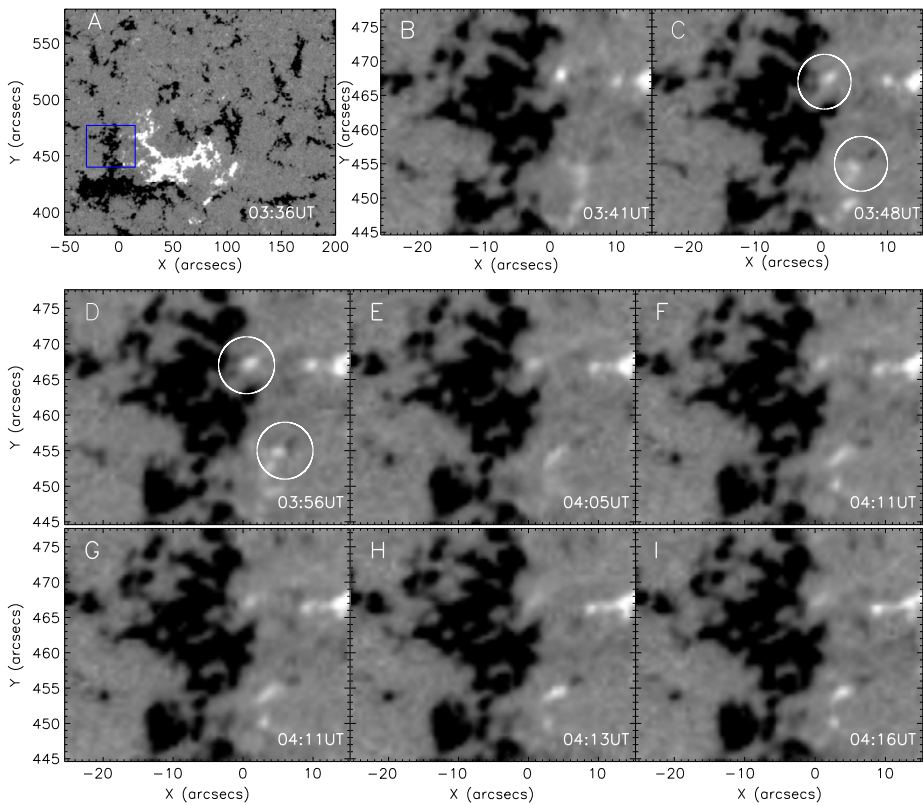
Figure 12   Panel **A** shows the line-of-sight magnetogram for a similar field of view as the top 171 Å images of Figure 11. The *boxed region* is the same region as shown in Figure 11, panel **A**. The zoomed versions of the *boxed region* of these magnetograms are displayed in a time sequence in which *circled regions* indicate zones of flux cancellation (panels **C** - **D**). An animation of the evolution of the magnetic field is available online (hmi.avi).

During the time period 03:45 to 04:21 UT, the expanding loops reached about $60''$ in height from their initial position with a projected speed of 20 ± 2.3 km s^{-1}, while the collapsing coronal loops came down by $35''$ with a projected speed of 12 ± 2.0 km s^{-1}. During the rise of the loop, a brightening was seen in the adjacent loop top. This brightened loop was cusp shaped, as shown by the white arrow labeled with an x in the sequence of 171 Å images in Figure 11 (panels **E** – **H**). The zoomed view of the green box (shown in Figure 11, panel H) can be seen in the 171, 304, and 193 Å wavelengths in panels a – f of Figure 11. The brightened cusp-shaped loop shown by an arrow x is visible in the 171 and 193 Å channels, but not in the 304 Å channel. The erupting filament is shown by an arrow labeled F2 in the 304 Å channel. The contour of the erupting filament extracted from the 304 Å channel (panel b) is overlaid on the 171 and 193 Å images and shows the position of the filament. The brightened loop was visible from $\sim 04{:}16$ UT until $\sim 04{:}27$ UT. The brightening might be due to the reconnection between the rising and overlying loops. At the same time, the filament activated and started to rise. The top coronal loop on the western side of the filament started to collapse at $\sim 03{:}59$ UT. The arrow labeled L3 in Figure 11 (panel C) shows the collapse of the coronal loops. Later, the filament rose higher and the overlying loop close to the western footpoint collapsed. While erupting, the filament appeared to be twisted

and eventually disappeared. In summary, on the east side of the filament, the loops moved upward and expanded. On the west side of the filament, the loops moved downward and shrank.

3.6. Magnetic Field Evolution

The magnetogram shows the filament location near the PIL of the two opposite-polarity plage regions (Figure 1, bottom-right panel). The HMI magnetogram movie (hmi.avi) shows the interaction and cancellation of opposite-polarity magnetic regions at the PIL. This region also showed a preflare brightening at around 01:56 UT on 27 March 2012. The flux cancellations near the PIL could be at the origin of the preflare brightening near the filament.

Figure 13 (left panel) shows the magnetogram a few minutes before the preflare brightening. The magnetic flux in the active region was computed within the contoured region shown in Figure 13 (left panel). This contour encloses the bipolar region of interest. Figure 13 (right panel) shows the calculated negative and positive fluxes for this contoured region. At $\sim 10{:}00$ UT on 26 March 2012, there was a slight difference in the magnetic flux of both polarities. The flux started to decrease in both polarities from the beginning of the observation. However, in the negative-polarity region, the flux clearly started to decrease after 16:00 UT. The flux decreased at a rate of $\sim 2.52 \times 10^{19}$ Mx h^{-1} in the positive-polarity region and at a rate of $\sim 5.89 \times 10^{19}$ Mx h^{-1} in the negative-polarity regions over a nine-hour period starting from 16:00 UT on 26 March 2012. When the flux decrease stopped, we observed the first filament eruption followed by the C5.3 class flare (shown by a dashed line in the plot). The second event occurred when there was a slight increase in negative flux and decrease in positive flux (shown by the solid line in the plot). The temporal evolution of the flux suggests that there were continuous flux cancellations in this region.

To explore the magnetic topology of the active region, we performed the potential field extrapolation using an HMI magnetogram at 00:04:00 UT on 27 March 2012. Figure 14 (left panel) displays the potential field source surface extrapolation (PFSS: Schrijver and De Rosa, 2003) of the active region. The white and pink lines indicate the closed and open field lines. The rotated view of the AR (toward the eastern limb) is shown in the right panel. The fan of loops emanates from the central positive-polarity region and connects to the surrounding opposite-polarity fields. The magnetic configuration is almost similar to a fan-spine topology (Pariat, Antiochos, and DeVore, 2010) with a possible magnetic null point.
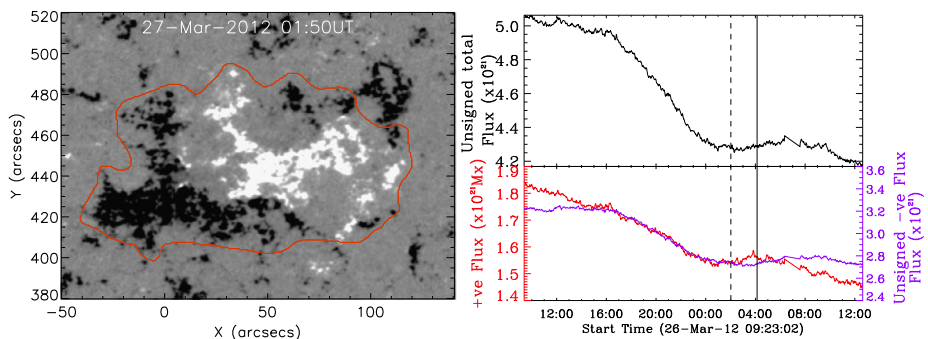

Figure 13 *Left*: Line-of-sight magnetogram of the region of interest. *Right*: calculated positive fluxes (*red*), unsigned negative fluxes (*blue*), and unsigned total fluxes (*black*) for the irregular contour. The *dashed* and *solid vertical lines* represent the onset time of the first and second filament eruptions, respectively.
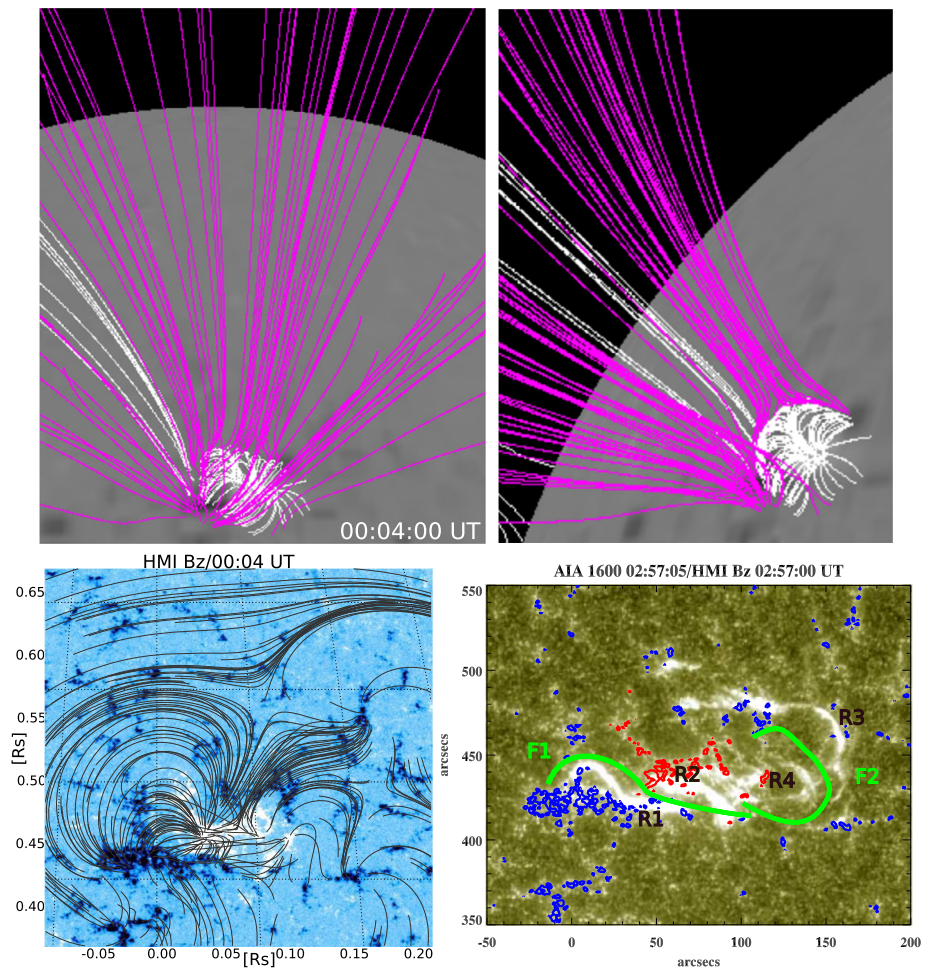
Figure 14 *Top-left*: potential field source surface extrapolation (PFSS) of AR NOAA 11444 at 00:04:00 UT on 27 March 2012. The *white* and *pink lines* indicate the closed and open field lines. The *top-right panel* shows the rotated view of the AR (toward the eastern limb). The *bottom-left panel* displays the NLFFF extrapolation of the field in a closer view. The *bottom-right panel* shows the AIA 1600 Å image during the appearance of flare ribbons due to the eruption of F1 at 02:57 UT. The flare ribbons are indicated as R1, R2, R3, and R4.

We used the vertical-current approximation non-linear force-free field (VCA–NLFFF: Aschwanden, 2016) code using SDO/HMI and SDO/AIA data to obtain a nonlinear force-free field solution of the magnetic field in an active region. We used the HMI line-of-sight magnetogram obtained at 00:04 UT and almost simultaneous six-channel AIA images (211, 193, 94, 131, 335, and 171 Å) as an input to determine the NLFFF solution. The bottom-left panel of Figure 14 displays the NLFFF extrapolation of the field lines in a closer view. We can see clear connectivities of the central positive-polarity region to the surrounding negative polarities, which is in agreement with the PFSS extrapolation. There seems to be a magnetic null point above the positive-polarity region, which is expected in a breakout magnetic topology.

The right panel shows the AIA 1600 Å image during the appearance of flare ribbons due to the eruption of F1 at 02:57 UT. We see several flare ribbons (R1, R2, R3, and R4). We draw the location of filaments F1 and F2 to show their association with the flare ribbons. Ribbons R1 and R2 are associated with F1, whereas R3 and R4 are associated with F2. However, F2 could not erupt during the first flare and was stopped by the overlying loop systems, as shown in the NLFFF extrapolation.

We note low-lying connecting loops above filament F1; no higher loops are observed above F1. However, we see higher closed fields above F2, where it was trapped during the first flare. Therefore, the NLFFF extrapolation suggests the role of the overlying magnetic fields in producing the successful and failed eruptions.

4. Summary and Discussion

We observed successive eruptions of filaments (F1 and F2) in AR NOAA 11444. The inverse J-shaped filament erupted in two different phases. In the first phase of the eruption, the southern portion of the filament erupted, while in the second phase the northern portion erupted. The summary of events is given in Table 1. These two eruption phases were accompanied by GOES C5.3 and C1.7 flares.

The transient brightening in EUV started at ∼01:56 UT below the filament, as discussed in Section 3.2, and it was followed by a bright plasma flow that moved from the east end of the filament to the west. The filament appeared as a sequence of bright and dark threads in 171 Å during the plasma flow. Photospheric magnetograms showed continuous cancellation of the flux near the PIL. The flux cancellation produced a jet below filament F1. Chae (2003) studied the formation of a reverse S-shaped filament in NOAA AR 8668 associated with a series of magnetic flux cancellations at the photosphere. The flux cancellations along the

Table 1 Summary of the events.

Time (UT)	Observation
∼01:56	A brightening was observed (green boxed region in Figure 1, top-right panel) in AIA 171, 193, 131, and 304 Å channels.
∼01:57–∼02:35	A bright flow was observed that moved from east to west of the filament.
∼02:30	One more brightening was observed near the east end of the filament. This brightening is related to the preflare brightening of a C5.3 class flare (see Figure 5) and the filament eruption (F1) starts.
∼02:32–∼02:35	Contraction of the coronal loop in the eastern part of the filament (see Figure 8).
∼02:53	C5.3 class flare along with the filament eruption (F1).
∼03:08	Peak time of the C5.3 class flare.
∼03:14	A dark filament portion appeared above the bright and dark filament channel (see Figure 9).
∼03:14–∼03:40	The northwest portion of the filament started to activate. Shrinking of one of the post-flare loops (L1) is visible (see Figure 9).
∼03:45	There was an expansion of loops (L2) upward at the east side of the filament. At the same time, a contraction of loops (L3) at the west side was also visible; these loops were located above the filament (see Figure 11).
∼04:16–∼04:26	A brightened cusp-shaped loop was observed near the east end of the filament, as shown by the arrow labeled as x in Figure 11 (panels E–H).
∼04:20	This filament eruption (F2) started, followed by a C1.7 class flare.

PIL can form the twisted helical flux rope that supports the filament, as formulated by van Ballegooijen and Martens (1989), and the same process can also destabilize the filament (Amari *et al.*, 2003; Martin and Livi, 1992). Before the eruption, filament F1 rose slowly at a velocity of $1.5 \pm 0.3 \ \mathrm{km\,s^{-1}}$. The slow rise of the filament started almost concurrently with the EUV brightening beneath F1. Later, it accelerated during the flare. A similar type of slow rise of a filament before eruption accompanied by an EUV brightening below it was reported by Sterling and Moore (2005). The authors interpreted their observations as the slow-rise phase of the eruption resulting from the onset of tether-cutting reconnection beneath the filament. The slow rise of the filament in the first phase of the eruption was most likely caused by tether-cutting reconnection (Moore and Roumeliotis, 1992; Sterling and Moore, 2005) caused by flux cancellation between the opposite-polarity magnetic fields below F1. The reconnection below F1 can reduce the tension of the overlying twisted fields and push F1 upward.

Sterling, Moore, and Freeland (2011) observed a gradual magnetic flux cancellation below a filament, which built the filament flux rope over time, causing it to rise gradually. The filament eventually erupted as a result of the onset of a magnetic instability and/or runaway tether cutting. During the onset and early development of the eruption for six bipolar events, Moore *et al.* (2001) observed that in each of the events the eruption was unleashed by runaway tether-cutting *via* reconnection in the middle of the sigmoid. As this internal reconnection starts at the beginning of the sigmoid eruption and grows together with it, their study suggests that this reconnection is essential for the onset and growth of magnetic eruption in eruptive flares and CMEs. Recent results also show direct observational evidence for the tether-cutting mechanism in at least two events (Chen *et al.*, 2014). The observed brightening near the low-lying filament end followed by a jet-like flow along the filament might indicate that magnetic reconnection occurred in the lower layers and might be a signature of the tether-cutting mechanism. This could have activated filament F1, which eventually erupted during the C5.3 class flare.

Furthermore, in the same active region, we observed a second phase of filament eruption (F2) after ~ 1.5 h of the first filament eruption (F1). We observed flux cancellations near the east side of the filament, where a small positive-polarity region interacted with the negative-polarity region. A brightening, followed by the rise of the loops, was observed at the same location. The eruption of the overlying loops above the filament could have removed a sufficient amount of overlying flux (as numerically explained by Török *et al.* (2011)), and facilitated the eruption of filament F2. For the same event, Lee *et al.* (2016) also explained that the eruption was possible because the topology of the dome-like magnetic fan structure above the AR was able to continue existing during the eruptions in spite of the significant changes in its geometry. The reason for the collapse of the loop observed near the western end of the filament is not clear. However, Liu and Wang, 2010 and Yan *et al.*, 2013 explained that the collapse of the loops might be due to the reduced magnetic pressure below the filament.

In summary, the filament eruption F1 is consistent with the following scenario. The gradual flux cancellation at the PIL resulted in the brightening, followed by the jet-like ejection below the filament main axis. The brightening could be due to the reconnection that occurred in the lower layers and might be a signature of the tether-cutting mechanism, which could have triggered the initial slow rise of filament F1 and its eventual eruption during the C5.3 class flare. However, filament F2 was trapped within the overlying loops and did not reach the height of the torus instability or loss of equilibrium, and it remained trapped for about 1.5 h. Filament F2 erupted after the overlying loops were removed. Both filament eruptions

were associated with two high-speed CMEs (1148 km s^{-1} [2] and 880 km s^{-1},[3] respectively), which were observed by the SOHO/LASCO and STEREO COR1 and COR2 coronagraphs. Future studies of successive filament eruptions with high-resolution observations would be helpful to understand the origin of the sequence of events that trigger them.

Disclosure of Potential Conflicts of Interest   The authors declare that they have no conflicts of interest.

References

Amari, T., Luciani, J.F., Aly, J.J., Mikic, Z., Linker, J.: 2003, Coronal mass ejection: initiation, magnetic helicity, and flux ropes, II: Turbulent diffusion-driven evolution. *Astrophys. J.* **595**, 1231. DOI. ADS.

Antiochos, S.K.: 1998, The magnetic topology of solar eruptions. *Astrophys. J. Lett.* **502**, L181. DOI. ADS.

Antiochos, S.K., DeVore, C.R., Klimchuk, J.A.: 1999, A model for solar coronal mass ejections. *Astrophys. J.* **510**, 485. DOI. ADS.

Aschwanden, M.J.: 2016, The vertical-current approximation nonlinear force-free field code description, performance tests, and measurements of magnetic energies dissipated in solar Flares. *Astrophys. J. Suppl. Ser.* **224**, 25. DOI. ADS.

Bateman, G.: 1978, *MHD Instabilities*, MIT Press, Cambridge.

Chae, J.: 2000, The magnetic helicity sign of filament chirality. *Astrophys. J. Lett.* **540**, L115. DOI. ADS.

Chae, J.: 2003, The formation of a prominence in NOAA active region 8668, II: Trace observations of jets and eruptions associated with canceling magnetic features. *Astrophys. J.* **584**, 1084. DOI. ADS.

Chen, P.F.: 2011, Coronal mass ejections: Models and their observational basis. *Living Rev. Solar Phys.* **8**, 1. DOI. ADS.

Chen, H., Zhang, J., Cheng, X., Ma, S., Yang, S., Li, T.: 2014, Direct observations of tether-cutting reconnection during a major solar event from 2014 February 24 to 25. *Astrophys. J. Lett.* **797**, L15. DOI. ADS.

Chifor, C., Tripathi, D., Mason, H.E., Dennis, B.R.: 2007, X-ray precursors to flares and filament eruptions. *Astron. Astrophys.* **472**, 967. DOI. ADS.

Dhara, S.K., Ravindra, B., Banyal, R.K.: 2014, Observations of photospheric vortical motions during the early stage of filament eruption. *Solar Phys.* **289**, 4481. DOI. ADS.

Fan, Y., Gibson, S.E.: 2007, Onset of coronal mass ejections due to loss of confinement of coronal flux ropes. *Astrophys. J.* **668**, 1232. DOI. ADS.

Forbes, T.G.: 2000, A review on the genesis of coronal mass ejections. *J. Geophys. Res.* **105**, 23153. DOI. ADS.

Gilbert, H.R., Alexander, D., Liu, R.: 2007, Filament kinking and its implications for eruption and reformation. *Solar Phys.* **245**, 287. DOI. ADS.

Gopalswamy, N., Shimojo, M., Lu, W., Yashiro, S., Shibasaki, K., Howard, R.A.: 2003, Prominence eruptions and coronal mass ejection: A statistical study using microwave observations. *Astrophys. J.* **586**, 562. DOI. ADS.

Green, L.M., Kliem, B., Wallace, A.J.: 2011, Photospheric flux cancellation and associated flux rope formation and eruption. *Astron. Astrophys.* **526**, A2. DOI. ADS.

Harvey, J.W., Hill, F., Hubbard, R.P., Kennedy, J.R., Leibacher, J.W., Pintar, J.A., Gilman, P.A., Noyes, R.W., Title, A.M., Toomre, J., Ulrich, R.K., Bhatnagar, A., Kennewell, J.A., Marquette, W., Patron, J., Saa, O., Yasukawa, E.: 1996, The global oscillation network group (GONG) project. *Science* **272**, 1284. DOI. ADS.

---

[2] http://cdaw.gsfc.nasa.gov/CME_list/UNIVERSAL/2012_03/htpng/20120327.031209.p346g.htp.html.

[3] http://cdaw.gsfc.nasa.gov/CME_list/UNIVERSAL/2012_03/htpng/20120327.042405.p097g.htp.html.

Hood, A.W., Priest, E.R.: 1979, Kink instability of solar coronal loops as the cause of solar flares. *Solar Phys.* **64**, 303. DOI. ADS.

Howard, R.A., Moses, J.D., Vourlidas, A., Newmark, J.S., Socker, D.G., Plunkett, S.P., Korendyke, C.M., Cook, J.W., Hurley, A., Davila, J.M., Thompson, W.T., St Cyr, O.C., Mentzell, E., Mehalick, K., Lemen, J.R., Wuelser, J.P., Duncan, D.W., Tarbell, T.D., Wolfson, C.J., Moore, A., Harrison, R.A., Waltham, N.R., Lang, J., Davis, C.J., Eyles, C.J., Mapson-Menard, H., Simnett, G.M., Halain, J.P., Defise, J.M., Mazy, E., Rochus, P., Mercier, R., Ravet, M.F., Delmotte, F., Auchere, F., Delaboudiniere, J.P., Bothmer, V., Deutsch, W., Wang, D., Rich, N., Cooper, S., Stephens, V., Maahs, G., Baugh, R., McMullin, D., Carter, T.: 2008, Sun earth connection coronal and heliospheric investigation (SECCHI). *Space Sci. Rev.* **136**, 67. DOI. ADS.

Kahler, S.W., Moore, R.L., Kane, S.R., Zirin, H.: 1988, Filament eruptions and the impulsive phase of solar flares. *Astrophys. J.* **328**, 824. DOI. ADS.

Kaiser, M.L., Kucera, T.A., Davila, J.M., St. Cyr, O.C., Guhathakurta, M., Christian, E.: 2008, The STEREO mission: An introduction. *Space Sci. Rev.* **136**, 5. DOI. ADS.

Karpen, J.T., Antiochos, S.K., DeVore, C.R.: 2012, The mechanisms for the onset and explosive eruption of coronal mass ejections and eruptive flares. *Astrophys. J.* **760**, 81. DOI. ADS.

Kim, S., Moon, Y.-J., Kim, K.-H., Kim, Y.-H., Sakurai, T., Chae, J., Kim, K.-S.: 2007, Two-step reconnections in a C3.3 flare and its preflare activity observed by Hinode XRT. *Pub. Astron. Soc. Japan* **59**, 831. ADS.

Kliem, B., Török, T.: 2006, Torus instability. *Phys. Rev. Lett.* **96**(25), 255002. DOI. ADS.

Kumar, P., Cho, K.-S.: 2014, Multiwavelength observation of a large-scale flux rope eruption above a kinked small filament. *Astron. Astrophys.* **572**, A83. DOI. ADS.

Kumar, P., Cho, K.-S., Bong, S.-C., Park, S.-H., Kim, Y.H.: 2012, Initiation of coronal mass ejection and associated flare caused by helical kink instability observed by SDO/AIA. *Astrophys. J.* **746**, 67. DOI. ADS.

Kusano, K., Bamba, Y., Yamamoto, T.T., Iida, Y., Toriumi, S., Asai, A.: 2012, Magnetic field structures triggering solar flares and coronal mass ejections. *Astrophys. J.* **760**, 31. DOI. ADS.

Lee, J., Liu, C., Jing, J., Chae, J.: 2016, Solar multiple eruptions from a confined magnetic structure. *Astrophys. J. Lett.* **829**, L1. DOI. ADS.

Lemen, J.R., Title, A.M., Akin, D.J., Boerner, P.F., Chou, C., Drake, J.F., Duncan, D.W., Edwards, C.G., Friedlaender, F.M., Heyman, G.F., Hurlburt, N.E., Katz, N.L., Kushner, G.D., Levay, M., Lindgren, R.W., Mathur, D.P., McFeaters, E.L., Mitchell, S., Rehse, R.A., Schrijver, C.J., Springer, L.A., Stern, R.A., Tarbell, T.D., Wuelser, J.-P., Wolfson, C.J., Yanari, C., Bookbinder, J.A., Cheimets, P.N., Caldwell, D., Deluca, E.E., Gates, R., Golub, L., Park, S., Podgorski, W.A., Bush, R.I., Scherrer, P.H., Gummin, M.A., Smith, P., Auker, G., Jerram, P., Pool, P., Soufli, R., Windt, D.L., Beardsley, S., Clapp, M., Lang, J., Waltham, N.: 2012, The atmospheric imaging assembly (AIA) on the solar dynamics observatory (SDO). *Solar Phys.* **275**, 17. DOI. ADS.

Liewer, P.C., de Jong, E.M., Hall, J.R., Howard, R.A., Thompson, W.T., Culhane, J.L., Bone, L., van Driel-Gesztelyi, L.: 2009, Stereoscopic analysis of the 19 May 2007 erupting filament. *Solar Phys.* **256**, 57. DOI. ADS.

Liu, R., Wang, H.: 2010, Fast contraction of coronal loops at the flare peak. *Astrophys. J. Lett.* **714**, L41. DOI. ADS.

Liu, W., Wang, T.-J., Dennis, B.R., Holman, G.D.: 2009, Episodic X-ray emission accompanying the activation of an eruptive prominence: Evidence of episodic magnetic reconnection. *Astrophys. J.* **698**, 632. DOI. ADS.

Liu, Y., Hoeksema, J.T., Scherrer, P.H., Schou, J., Couvidat, S., Bush, R.I., Duvall, T.L., Hayashi, K., Sun, X., Zhao, X.: 2012, Comparison of line-of-sight magnetograms taken by the solar dynamics observatory/helioseismic and magnetic imager and solar and heliospheric observatory/michelson doppler imager. *Solar Phys.* **279**, 295. DOI. ADS.

Martin, S.F.: 1980, Preflare conditions, changes and events. *Solar Phys.* **68**, 217. DOI. ADS.

Martin, S.F.: 1998, Conditions for the formation and maintenance of filaments (invited review). *Solar Phys.* **182**, 107. DOI. ADS.

Martin, S.F., Bilimoria, R., Tracadas, P.W.: 1994, Magnetic field configurations basic to filament channels and filaments. In: Rutten, R.J., Schrijver, C.J. (eds.) *NATO Adv. Sci. Inst. Ser. C* **433**, 303. ADS.

Martin, S.F., Livi, S.H.B.: 1992, The role of cancelling magnetic fields in the buildup to erupting filaments and flares. In: Svestka, Z., Jackson, B.V., Machado, M.E. (eds.) *IAU Colloq. 133: Eruptive Solar Flares*, *Lect. Notes Phys.* **399**, 33. ADS.

Martin, S.F., Livi, S.H.B., Wang, J.: 1985, The cancellation of magnetic flux, II: In a decaying active region. *Aust. J. Phys.* **38**, 929. ADS.

Moore, R.L., Labonte, B.J.: 1980, The filament eruption in the 3B flare of July 29, 1973 – onset and magnetic field configuration. In: Dryer, M., Tandberg-Hanssen, E. (eds.) *IAU Symp. 91: Solar and Interplanetary Dynamics*, 207. ADS.

Moore, R.L., Roumeliotis, G.: 1992, Triggering of eruptive flares – destabilization of the preflare magnetic field configuration. In: Svestka, Z., Jackson, B.V., Machado, M.E. (eds.) *IAU Colloq. 133: Eruptive Solar Flares*, *Lect. Notes Phys.* **399**, 69. ADS.

Moore, R.L., Sterling, A.C.: 2006, Initiation of coronal mass ejections. *AGU Geophys. Monograph Ser.* **165**, 43. ADS.

Moore, R.L., Sterling, A.C., Hudson, H.S., Lemen, J.R.: 2001, Onset of the magnetic explosion in solar flares and coronal mass ejections. *Astrophys. J.* **552**, 833. DOI. ADS.

Nagashima, K., Isobe, H., Yokoyama, T., Ishii, T.T., Okamoto, T.J., Shibata, K.: 2007, Triggering mechanism for the filament eruption on 2005 September 13 in NOAA active region 10808. *Astrophys. J.* **668**, 533. DOI. ADS.

Pariat, E., Antiochos, S.K., DeVore, C.R.: 2010, Three-dimensional modeling of quasi-homologous solar jets. *Astrophys. J.* **714**, 1762. DOI. ADS.

Pesnell, W.D., Thompson, B.J., Chamberlin, P.C.: 2012, The solar dynamics observatory (SDO). *Solar Phys.* **275**, 3. DOI. ADS.

Priest, E.R., Forbes, T.G.: 2002, The magnetic nature of solar flares. *Astron. Astrophys. Rev.* **10**, 313. DOI. ADS.

Priest, E.R., Parnell, C.E., Martin, S.F.: 1994, A converging flux model of an X-ray bright point and an associated canceling magnetic feature. *Astrophys. J.* **427**, 459. DOI. ADS.

Scherrer, P.H., Schou, J., Bush, R.I., Kosovichev, A.G., Bogart, R.S., Hoeksema, J.T., Liu, Y., Duvall, T.L., Zhao, J., Title, A.M., Schrijver, C.J., Tarbell, T.D., Tomczyk, S.: 2012, The helioseismic and magnetic imager (HMI) investigation for the solar dynamics observatory (SDO). *Solar Phys.* **275**, 207. DOI. ADS.

Schmieder, B., van Driel-Gesztelyi, L., Aulanier, G., Démoulin, P., Thompson, B., de Forest, C., Wiik, J.E., Saint Cyr, C., Vial, J.C.: 2002, Relationships between CME's and prominences. *Adv. Space Res.* **29**, 1451. DOI. ADS.

Schrijver, C.J., De Rosa, M.L.: 2003, Photospheric and heliospheric magnetic fields. *Solar Phys.* **212**, 165. DOI. ADS.

Srivastava, A.K., Zaqarashvili, T.V., Kumar, P., Khodachenko, M.L.: 2010, Observation of kink instability during small B5.0 solar flare on 2007 June 4. *Astrophys. J.* **715**, 292. DOI. ADS.

Sterling, A.C., Harra, L.K., Moore, R.L.: 2007, New evidence for the role of emerging flux in a solar filament's slow rise preceding its CME-producing fast eruption. *Astrophys. J.* **669**, 1359. DOI. ADS.

Sterling, A.C., Moore, R.L.: 2005, Slow-rise and fast-rise phases of an erupting solar filament, and flare emission onset. *Astrophys. J.* **630**, 1148. DOI. ADS.

Sterling, A.C., Moore, R.L., Freeland, S.L.: 2011, Insights into filament eruption onset from solar dynamics observatory observations. *Astrophys. J. Lett.* **731**, L3. DOI. ADS.

Sterling, A.C., Chifor, C., Mason, H.E., Moore, R.L., Young, P.R.: 2010, Evidence for magnetic flux cancelation leading to an ejective solar eruption observed by Hinode, TRACE, STEREO, and SoHO/MDI. *Astron. Astrophys.* **521**, A49. DOI. ADS.

Toriumi, S., Iida, Y., Bamba, Y., Kusano, K., Imada, S., Inoue, S.: 2013, The magnetic systems triggering the M6.6 class solar flare in NOAA active region 11158. *Astrophys. J.* **773**, 128. DOI. ADS.

Török, T., Kliem, B.: 2003, The evolution of twisting coronal magnetic flux tubes. *Astron. Astrophys.* **406**, 1043. DOI. ADS.

Török, T., Kliem, B., Titov, V.S.: 2004, Ideal kink instability of a magnetic loop equilibrium. *Astron. Astrophys.* **413**, L27. DOI. ADS.

Török, T., Panasenco, O., Titov, V.S., Mikić, Z., Reeves, K.K., Velli, M., Linker, J.A., De Toma, G.: 2011, A model for magnetically coupled sympathetic eruptions. *Astrophys. J. Lett.* **739**, L63. DOI. ADS.

van Ballegooijen, A.A., Martens, P.C.H.: 1989, Formation and eruption of solar prominences. *Astrophys. J.* **343**, 971. DOI. ADS.

Wang, J., Shi, Z.: 1993, The flare-associated magnetic changes in an active region. II: Flux emergence and cancellation. *Solar Phys.* **143**, 119. DOI. ADS.

Xu, Y., Jing, J., Wang, H.: 2010, Measurements of filament height in Hα and EUV 304 Å. *Solar Phys.* **264**, 81. DOI. ADS.

Yan, X.L., Pan, G.M., Liu, J.H., Qu, Z.Q., Xue, Z.K., Deng, L.H., Ma, L., Kong, D.F.: 2013, The contraction of overlying coronal loop and the rotating motion of a sigmoid filament during its eruption. *Astron. J.* **145**, 153. DOI. ADS.

Yan, X.L., Xue, Z.K., Liu, J.H., Ma, L., Kong, D.F., Qu, Z.Q., Li, Z.: 2014, Kink instability evidenced by analyzing the leg rotation of a filament. *Astrophys. J.* **782**, 67. DOI. ADS.

Young, C.A.: 2007, Mkit: An IDL multiscale toolbox. *Bull. Amer. Astron. Soc.* **39**, 133. ADS.

Zuccarello, F., Battiato, V., Contarino, L., Romano, P., Spadaro, D.: 2007, Plasma motions in a short-lived filament related to a magnetic flux cancellation. *Astron. Astrophys.* **468**, 299. DOI. ADS.

Zuccarello, F.P., Seaton, D.B., Mierla, M., Poedts, S., Rachmeler, L.A., Romano, P., Zuccarello, F.: 2014, Observational evidence of torus instability as trigger mechanism for coronal mass ejections: The 2011 August 4 filament eruption. *Astrophys. J.* **785**, 88. DOI. ADS.